Biomass Conversion and Biorefinery
https://doi.org/10.1007/s13399-024-05413-8

ORIGINAL ARTICLE

Semi-conductive carbon from industrial tea waste biomass for a p-n junction

Gökçen Akgül[1] · **Murat Tomakin**[2] · **Hasan Hüseyin Erkaya**[3]

Received: 8 November 2023 / Revised: 18 January 2024 / Accepted: 7 February 2024

Abstract
Some semiconducting carbonaceous material was developed from industrial tea waste biomass by catalytic pyrolysis and heteroatom doping; then, a p-n junction was realized on an n-type Si substrate. I-V characteristics of the structures revealed that each structure had a different reverse saturation current, ideality factor, cut-in voltage and series resistance. The variations in the characteristics are attributed to the amorphous and non-uniform nature of the carbonaceous material. Due to the high resistivity of the carbonaceous material, a significant amount of series resistance was present in the characteristics, resulting in very small levels of current that would inhibit the practical use of the structure as a semiconductor diode in electronic circuits.

Keywords Biomass · Tea waste · Semiconductive carbonaceous materials · p-n junction

Abbreviations

α	Absorbance coefficient
d	Thickness of the film
E_g	Band gap energy
h	Planck constant
ν	Frequency of light
c	Velocity of light
λ	Wavelength
I	Current
I_s	Reverse saturation current
V	Voltage
n	Ideality factor
q	Charge
k_B	Boltzmann constant
T	Temperature
V_T	Thermal voltage
I_s	Reverse saturation current
V_γ	Cut-in voltage
R_F	Forward series resistance
ε_r	Permittivity of medium
ε_o	Permittivity of free space
τ_r	Relaxation time
σ	Conductivity
ω	Frequency
R	Resistance
C	Capacitance
ρ	Resistivity
$A(x)$	Cross sectional area
A_c	Area of capacitor
x_n	Depletion region width on the Si layer
x_p	Depletion width on the carbon layer
N_D	Doping density on Si layer
N_A	Doping density on carbon layer
V_b	Band bending voltage
V_{an}	Fraction of applied voltage
$\|Q^-\|$, $\|Q^+\|$	Space charges

✉ Gökçen Akgül
gokcen.akgul@erdogan.edu.tr

✉ Hasan Hüseyin Erkaya
hherkaya@ogu.edu.tr

[1] Department of Energy Systems Engineering, Engineering and Architecture Faculty, Recep Tayyip Erdogan University, 53100 Rize, Turkey

[2] Department of Physics, Faculty of Art and Science, Recep Tayyip Erdogan University, 53100 Rize, Turkey

[3] Electrical-Electronics Engineering Department, Faculty of Engineering and Architecture, Eskisehir Osmangazi University, Bati Meselik, 26480 Eskisehir, Turkey

1 Introduction

The comfort of human life is gradually increasing with the automation of machines, which is the result of developing electronic technology. Electronics are everywhere, ranging from amplifiers to smart internet for everything components. As materials, semiconductor materials are the heart of

Published online: 17 February 2024

electronic devices, finding place in about whole electronic entities.

The commonly manufactured and best-known semiconducting materials are elemental silicon and germanium, as well as various composites such as gallium arsenide, indium phosphide and cadmium sulfide [1]. Meanwhile, studies on material development in semiconductor technology are still ongoing. Recently, graphitic-structured and nano-sized carbon-based semiconductor technology is among the very popular research themes in regard to manufacturing lightweight, flexible, miniaturized, thermally stable and cost-effective new generation electrical/electronic devices such as foldable cell phones, interconnects, chips, wearable gadgets, transistors, antennas, solar cells, light emitting diodes or sensors [2]. For example, Graham et al. [3] presented the integration of carbon nanotubes (CNT) into microelectronic devices carrying more current and flexibility. According to Zamzami et al. [4], they made a field effect-CNT transistor (FET-CNT) using the photolithography method and found that CNT acts as an effective semiconducting material on the sensing channels. Zhang et al. [5] generated metal-free ultraviolet light emitting diodes (UV-LED) with carbon nanodots, which are the new stars in carbon nanomaterials. CNT upon photodetector is realized with GaAs bulk semiconductor-based p-n heterojunction, promoting ultrahigh carrier mobility in the photodetector [6].

There are challenges with carbon nanomaterials in electrical/electronic implementations. First, there are technical difficulties in achieving the desired quality through the synthesis processes. Second, the carbon nanomaterials are mass-produced mostly from fossil sources of coal, gas or oil [7, 8]. In the era of sustainable and clean carbon technology in electric/electronics, renewable, alternative, biodegradable and eco-friendly new carbon resources are required.

Biomass would be the answer to offering renewable and sustainable carbon nanomaterials in semiconductor technology. Xu et al. [9] reviewed the valorization of the bio waste into carbon nanomaterials/bio (nano) materials (fullerenes, graphitic carbon, graphene, graphene- like porous carbons, carbon dots and CNT) in the waste-to-wealth concept. Tiwari et al. [10] and Tamuly et al. [11] presented the conversion of biomass into the value-added carbon nanomaterials, mostly through pyrolytic treatments. These materials have the potential to be utilized as adsorbents, solar cells or photocatalysts [12–14] or practiced as LEDs [15, 16]. The biomass-based metal-free semiconductor photocatalyst is described as an environmentally friendly application to solve water and air purification issues. The electron with an energy exceeding the band gap energy moves towards the semiconductor surface and initiates a series of redox reactions in the purification. Villarreal et al. [14] reviewed the renewable carbon materials for bio-sensitized, biodegradable, lightweight, flexible solar cell devices. The main advantages of renewable carbon materials over metal oxide semiconductor materials are stated as scalable photoelectronic phenomena. In another work, a white light LED chip is developed using carbon nanodots derived from mango leaf biomass [16]. There would be similar works in the literature; however, there is a lack of p-n junction formation on such semiconductive carbonaceous material from biomass [17].

In this work, semiconducting carbonaceous material is developed from industrial tea waste biomass through catalytic pyrolysis and heteroatom doping. A p-n junction is realized with the carbonized material on an n-type Si substrate, then the electrical characterization of the material and the junction is carried out. The novelty of this work is the derivation and extraction of refined carbon towards graphene-like carbon from biomass as a renewable carbon resource instead of fossil sources and the application of it to form a p-n junction to investigate and develop material for the evaluation of biomass as a value-added technological product.

2 Experimental

2.1 Development of p-type carbon from tea waste biomass

The detailed method to develop the refined carbonaceous material from tea waste can be found elsewhere [18]. Briefly, the tea waste was collected from a local tea processing plant, dried and grinded to 0.5 mm. Then, it was impregnated with a graphitization agent of saturated $FeCl_3$ in water in a 2:1 (w/w) ratio (TW: $FeCl_3$). The dry sample was pyrolyzed in a rotary oven (Protherm RTR 11/100/500) at 850 °C for 1 h in the inert atmosphere of N_2 with a 1 L/min flow rate and ~10 °C/min heating rate. The carbonized sample (BC-Fe, BC refers to "Bio Carbon") was washed tightly with 6 M HCl and 6 M HF to remove the impregnated metal oxides and the other possible minerals in the biomass (BC-Fe-Y). KOH as an activating agent was impregnated to BC–Fe–Y as carbonized sample:KOH with ratios of 1:4 and 1:2 (w/w). The dry impregnated samples were pyrolyzed a second time at 850 °C for 15 min in the inert atmosphere of N_2 with 1 L/min flow rate with a rapid heating rate of ~35 °C/min. The KOH activated samples were washed after pyrolysis with diluted HCl and water to neutralize them, then dried. The samples were identified as BC–Fe–Y–KOH1 (1:4 ratio) and BC–Fe–Y–KOH2 (1:2 ratio). The optimum KOH activation ratio was determined to be 1:2 with a higher surface area. The boron doping to obtain p-type material was realized with BC–Fe–Y–KOH2 by saturated aqueous H_3BO_3 solution in 1:1 and 2:1 ratios (w/w, carbonized sample: H_3BO_3) to BC–Fe–Y–KOH2. The dried samples were heated at 200 °C for 3 h to obtain BC–Fe–Y–KOH2–B1 and BC–Fe–Y–KOH2–B2, respectively. These two p-type end-products are shortly nomenclatured as B1 and B2, and their p-n junctions were realized

with an n-type Si substrate. The experimental flowchart is given in Fig. 1. The XRD analyses were performed by Rigaku Smart-Lab X-ray diffractometer non-monochromatographic CuKα1-radiation (40 kV, 30 mA, $\lambda = 1.54$ Å.

2.2 Electrical and optical characterizations of the derived materials

The resistivities and carrier densities of carbon materials were determined from sample films deposited on a 1 cm × 1 cm glass substrate (microscope lamella glass, cleaned with the RCA method) by the Van der Pauw four-point method and Hall effect measurements at 4750 Gauss magnetic field created by a DC source (Uni-T UTP3315TFL), respectively. Small-area four-point ohmic contacts were formed on the carbon film in the corners of the samples with indium solder for measurements. The method involves passing current between two contacts and measuring the voltage between the other two contacts. A series of measurements are made, and cross-resistances are calculated as the ratios of voltages to currents. Then, the resistivity of the film is calculated according to the method suggested. For the Hall effect measurements, a magnetic field perpendicular to the film surface is applied. Then, a current is passed between two opposing contacts. The magnetic field applies the Lorentz force on the carriers, which makes the carriers accumulate close to the other contacts—positive charge on one side and the negative charge on the other side. This uneven charge distribution creates an electric field that is perpendicular to both directions of the current and the magnetic field. This field creates the Hall voltage that is measured between the two cross contacts. From these voltage, carrier densities are determined. The detailed calculation procedure can be found elsewhere [19] and is given as Supplementary data in this work.

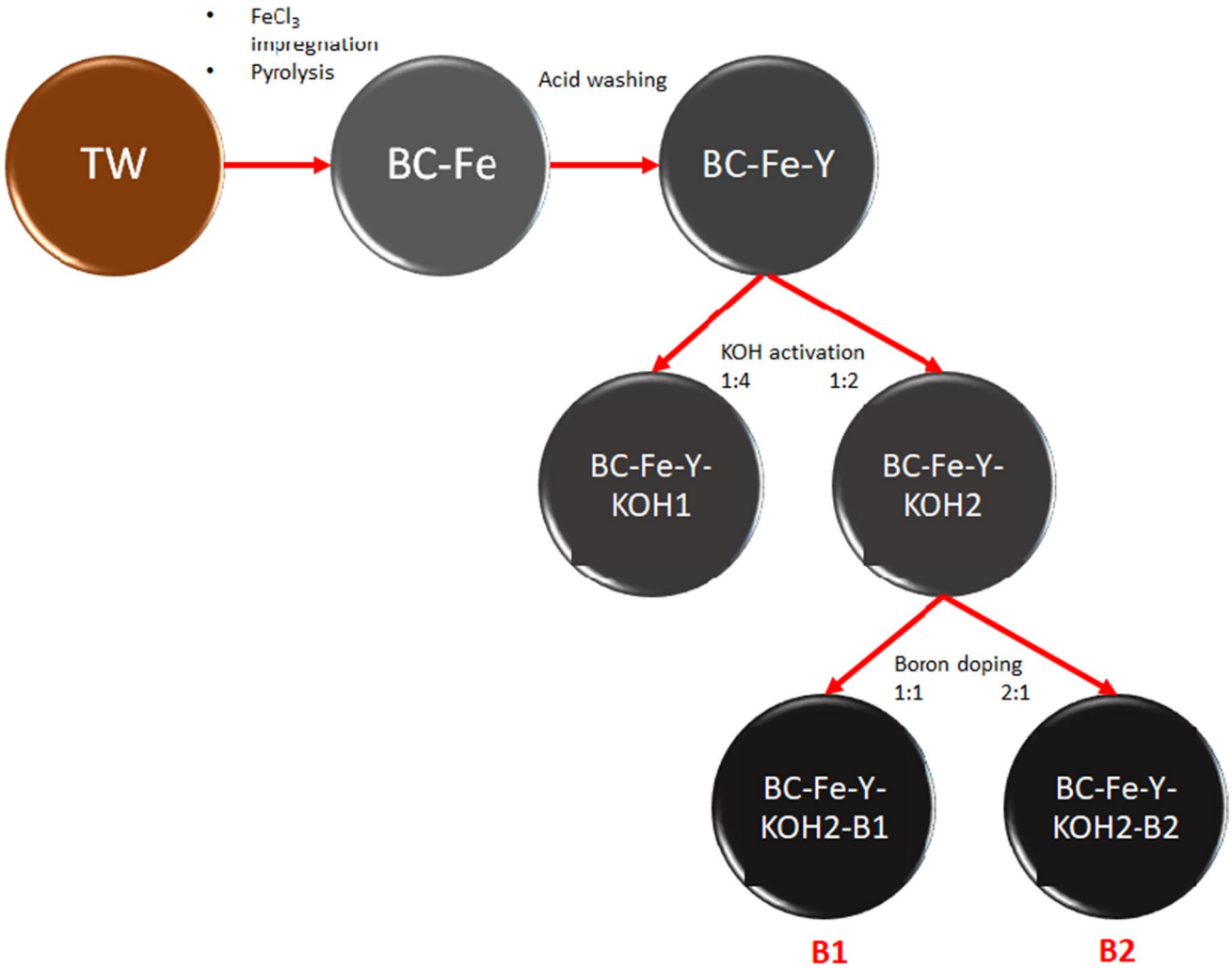

Fig. 1 The derivation pathway of investigated carbonized material from tea waste biomass

For the optical measurements of the samples on the glass substrate, a wavelength range of 300–1000 nm was used by the Spectramax M5 spectrophotometer, and the results were evaluated to calculate the energy band of the samples by the Tauc method.

2.3 p-n junction on silicon substrate and characterization

The p-n junction was prepared by placing a solution containing the p-doped carbonaceous material onto an n-type silicon substrate (Crystec, n-type Si/SiO_2, 3 inches, 380 µm (100) orientation, 1–10 Ω cm specific resistance, 2×10^{14}–10^{17} cm^{-3} doping density, 0.5 cm × 0.5 cm, cleaned with the RCA method [29]) and then heating them. For this purpose, 1 g of p-type carbon sample (B1 or B2) was dissolved in 20 ml of N-methyl pyrrolidone (NMP) solution treated in an ultrasonic bath (Elma S 50R) for 45 min and centrifuged at 5000 rpm for 30 min (Universal 320R, Hettich Zentrifugen). The supernatant (~20 µl) was placed by a micropipette onto the n-type Si substrate on a heated hot plate at 80 °C. Before placing the material, the Si substrate was etched with 2 M HF and water by plunging into the liquids. The prepared junctions were annealed at 550 °C for 1 h in an oven (Nevola) to consolidate the organic bindings between Si and carbon surfaces. Three structure samples were prepared for each carbon run. The prepared junctions were nomenclatured as JB1 and JB2.

The current-voltage (I-V) characteristics of the junctions were determined by the source meter (Keithley 2410) and the Labview-2011 screening program at a scanning speed of 0.1 V/s with the mechanical contacts of indium (plate)/n-Si/p-type carbon layer (B(x))/Ag (Fig. 2).

The surface morphology of the junctions and the film thicknesses were examined by scanning electron microscopy (SEM-EDX, Jeol JSM-6610). The capacitance–voltage (C–V) characteristics of the p-n junctions were obtained using a Wayne Kerr 6500B impedance analyzer in the 100 kHz–10 MHz frequency range and −2 to +2 V bias range.

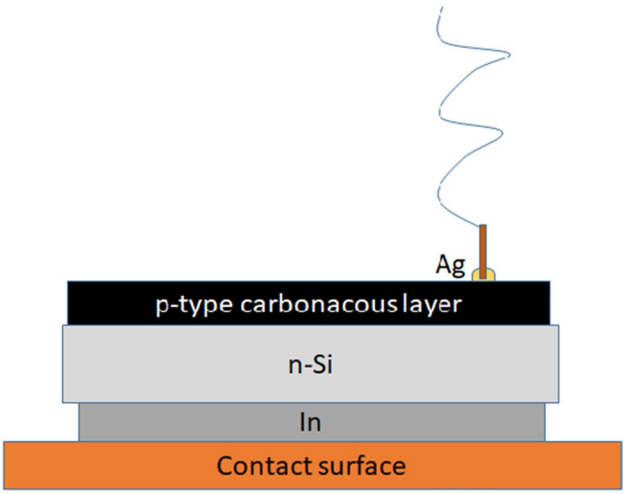

Fig. 2 The I-V measurement setup

3 Results and discussion

3.1 Structural characterizations of carbonaceous materials

The structural characterizations of the carbonaceous samples are discussed in detail elsewhere [18]. The heteroatom contents of the samples are determined to be 50 and 41% for B1 and B2, respectively, while the mineral content is less than 3%. The carbonaceous side of the samples is rich in the main surface groups such as OH, C–H, C=C, COOH and CO. The surface areas of the B1 and B2 are 119 m^2g^{-1} and 358 m^2g^{-1}, respectively. The derived carbonaceous materials consist of mainly amorphous structures but also contain some ordered graphitic parts [20] including boron, which can be extracted by dissolving it in the NMP solvent [21, 22]. The XRD analyses of the NMP-extracted B1, B2 and a reference graphite on the glass substrate are given in Fig. 3. The general view of the peaks indicates the amorphous structures. The main broad peaks at 24° (002) is responsible for carbon. These results could only be helpful to confirm the extracting of the carbon by NMP which was later settled on the Si substrate of junctions. The BC-derived samples show similar amorphous XRD behavior to the reference graphite.

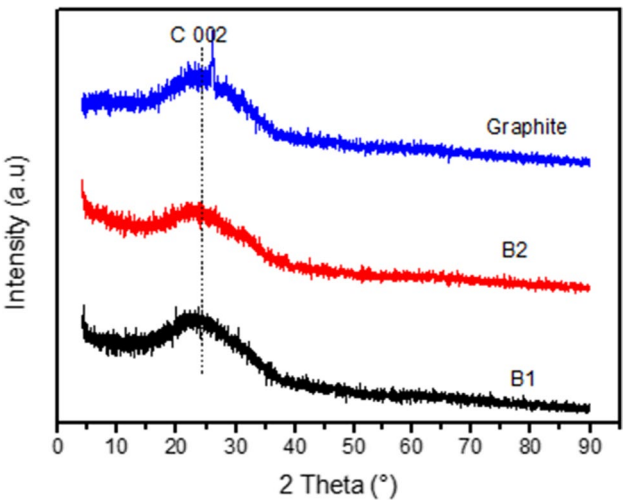

Fig. 3 XRD analyses of B1, B2 and a reference graphite material on glass substrate

3.2 Optical and electrical characterizations of the biomass derived materials

The electrical resistivities and carrier densities of the carbonaceous samples in this work are determined as 4.6×10^{4} Ω cm and 5.2×10^{4} Ω cm and 1.1×10^{13} cm^{-3} and 9.5×10^{12} cm^{-3} for the samples B1 and B2, respectively. In the previous studies, the electrical resistivities and carrier densities of the chemically derived reduced graphene oxide (rGO), chemically exfoliated sample of BC–Fe–Y (BC–Fe–Y–rR) and the carbonaceous sample BC–B–Y–KOH2–B2 which are developed by the same method with the difference of boric acid as graphitization agent [16, 18, 19] were found as 3.2×10^{3} Ω cm, 3.3×10^{3} Ω cm and 1.2×10^{6} Ω cm while the carrier densities are 6.8×10^{14} cm^{-3}, 1.0×10^{14} cm^{-3} and 5.8×10^{11} cm^{-3}, respectively. The resistivities of the carbonaceous materials derived in this work are about the same size. This means that the structural development of biomass-derived carbonaceous materials into oriented carbon sheets leads to better electrical conductivity.

Optical measurement is one of the effective methods for calculating the band gap energy (E_g) between the conduction band and the valence band of semiconductor materials. The E_g is determined by the relationship with the absorbance coefficient (α) given in Eq. 1:

$$\alpha = -\ln\left(\frac{1}{T}\right)\frac{1}{d} \tag{1}$$

where α is the absorbance coefficient (1/transparency), d is the thickness of the film (~2 μm) and T is the transmittance. The optical transparency measurements of the carbonaceous samples are shown in Fig. 4. The dip around 360 nm could be a result of the π-conjugated structures [18].

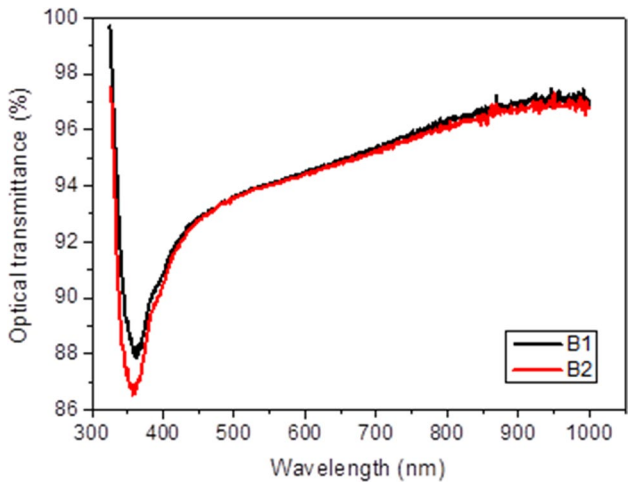

Fig. 4 The optical transmittances of the carbonaceous samples

The graph of $(\alpha h\nu)^2$ versus $h\nu$ would yield the value of E_g as given in Fig. 4, where h is the Planck constant, ν is the frequency (c/λ, c is the velocity of light, and λ is the wavelength of the scanning light). Both curves of the samples are very close, bringing out similar E_g values of approximately 2.25 eV for B1 and B2. The band gap energies of the materials are consistent for semiconductors [18].

The electrical properties of the bio-carbon samples are summarized in Table 1. Comparing with the previous studies, the electrical conductivities of $FeCl_3$ graphitized samples are higher than those of boron graphitized ones, which can be the result of a better structural ordering towards graphitic sheets (Fig. 5) rather than gemmiferous one like BC-B-Y-KOH2-B2 [17]. The electrical conductivity and carrier density of B1 and B2 advance on the values to rGO are around 100 times higher than the boron graphitized one. The higher heteroatom doping seems only to contribute to a slightly higher carrier density, probably due to more p-content. Furthermore, the resistivity of the n-type substrate here is 1–10 Ω cm. Then, the film resistivity of the samples seems to be ~5×10^{3}–5×10^{4} times higher and accordingly has lower carrier density than silicon.

3.3 Characteristics of the p-n junctions

Figure 6 shows the SEM-EDS analyses of the junctions where a splayed sample morphology like a cloth is seen on the Si surface for both samples (Fig. 6a, d) although it seems not homogenous. The EDS layers (Fig. 6b, e) present the distribution of three atoms of oxygen, boron and carbon on the surface. Both JB1 and JB2 junction surfaces are rich in oxygen, which is analyzed by the map sum spectrum (Fig. 6c, f) on the cross section as higher than 60% wt. The spreading of boron among the carbon structure is seen in EDS layers as well. Continued morphology would ensure that electrons are continuously transferred to the surface. In the previous study [17], a crumbled morphology of the sample BC–B–Y–KOH2–B2 was pictured which would result in less electrical conductivity than in this work. The samples are rich in oxygen atoms, as shown in the EDS results, which are consistent with the FTIR analyses in [18] which would cause a higher resistivity compared with rGO for the samples in this work. It is most likely that H_3BO_3 turns to its oxidized forms as well.

3.3.1 Current-voltage characteristics of the p-n junctions

Three junction devices were cut (5 mm × 5 mm) from JB1 and JB2 and labeled as JB1-1, JB1-2, JB1-3, JB2-1, JB2-2 and JB2-3. Then, the I-V characteristics of the p-n junctions were determined (Fig. 7). The use of Ag paste to contact

Table 1 Electrical characteristics of carbonaceous materials and resulting device parameters

Sample	Resistivity (Ω cm)	Carrier density (cm^{-3})	Film thickness (μm)	Type	Band gap energy (eV)	n	I_s (μAcm^{-2})	Reference
Si	10^{-3}–10^{2}	10^{14}–10^{20}		–	1.1–1.7			
rGO	3.2×10^{3}	6.8×10^{14}	~0.15	–	2.26 2.2			[19] [23]
BC–Fe–Y–rR	3.3×10^{3}	1.0×10^{14}	~0.15	–	2.37			
BC–B–Y–KOH2–B2	1.2×10^{6}	5.8×10^{11}	~15	p	–	14.08	0.035	[17]
B1	4.6×10^{4}	1.1×10^{13}	~2	p	~2.25	~5.04	~2.72	This work
B2	5.2×10^{4}	9.5×10^{12}	~2	p	~2.25	~6.54	~2.72	
Graphite	~0	11×10^{18}	–	–	~0			[24]

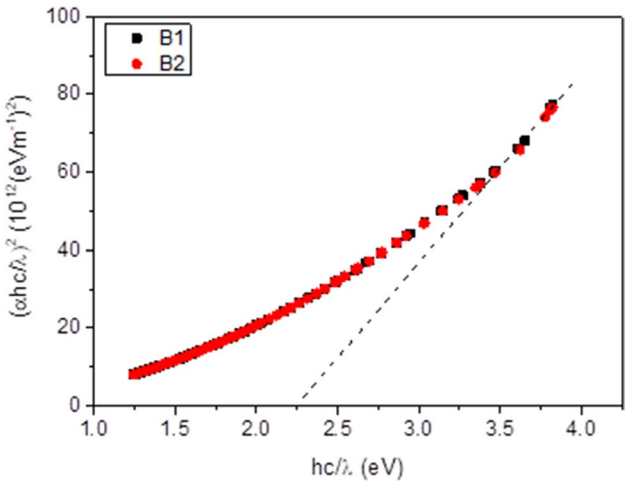

Fig. 5 The E_g of the samples is determined by the intercept of the extrapolation of the linear portion of the curve and the lateral axis

the BC layer for the I-V characteristics seemed to cause inconsistent results. This inconsistent behavior could be due to some silver paths reaching the substrate through the BC layer via pinholes that are present in the BC layer. Therefore, the I-V measurements were performed with direct contact of the probe to the BC layer without any silver paste, providing more reliable curves. Each measurement from the same batch seems to provide a different characteristic curve. The characteristics can be analyzed with a non-linear/exponential model and a piecewise linear model on the forward bias side, taking two experimental points on each curve.

The I-V relationship can be evaluated by classical diode Eq. 2:

$$I = I_s\left(e^{\frac{V}{n\,V_T}} - 1\right) \tag{2}$$

where I is the current; I_s, the reverse saturation current; V, the applied voltage; n, ideality factor; $V_T = k_B.T/q$, the thermal voltage where q is the charge on an electron; k_B, the Boltzmann constant; T, the temperature. At 300 K, the value of the thermal voltage is ~26 mV. Using two experimental points on the forward bias part of each curve, the ideality factor and the reverse saturation current can be calculated.

For the piecewise linear model—that would be more practical from a circuits point of view—the same experimental points may be used to obtain a cut-in voltage (V_γ) and a forward series resistance (R_F). For the analytical calculations, the exponential in Eq. 2 is assumed to be dominant. The referred graphs are given in Fig. 7; the results are presented in Table 2.

JB2-1 curve seems to have two distinct parts. The reverse saturation current (I_s) can be estimated from the semilog plot of the I-V curve by extrapolating the "linear" portion of the curves with a straight line to intercept the current axis at zero voltage. Likewise, the cut-in voltage (V_γ) can be read from the linear graph in Fig. 7a, b by extrapolating the "linear" portion of the curves with a straight line to intercept the voltage axis at zero current. The forward resistance R_F is estimated from the slope of this line. The estimated diode parameters are summarized in Table 3.

Each sample structure seems to have a different "diode" curve. Each curve has a different cut-in voltage and reverse saturation current. The forward series resistance, too, varies for each structure. The curve that had a 0.2-V cut-in voltage (JB2-1) resembles that of a Schottky diode (metal/semiconductor rectifying junction) on silicon, whose cut-in voltage is often approximated to be 0.4 V in electronic circuits. It could be due to carbon acting as a "conductor" on the surface of the silicon substrate. As for the variation of cut-in voltages of the other structures, the amorphous nature of the BC layer and possible structural non-uniformity in it could result in dissimilar diode characteristics. The general occurrence of lower cut-in voltages of JB2 than JB1 would partly be the result of higher resistivity in the device.

The measured current levels are extremely small for the structures. This is basically due to the high resistivity in the BC layers posing itself as a significant series resistance. The point contact on the top BC layer and large surface contact to the silicon substrate on the bottom introduce a shape factor that would add to the series resistance. Some portion of

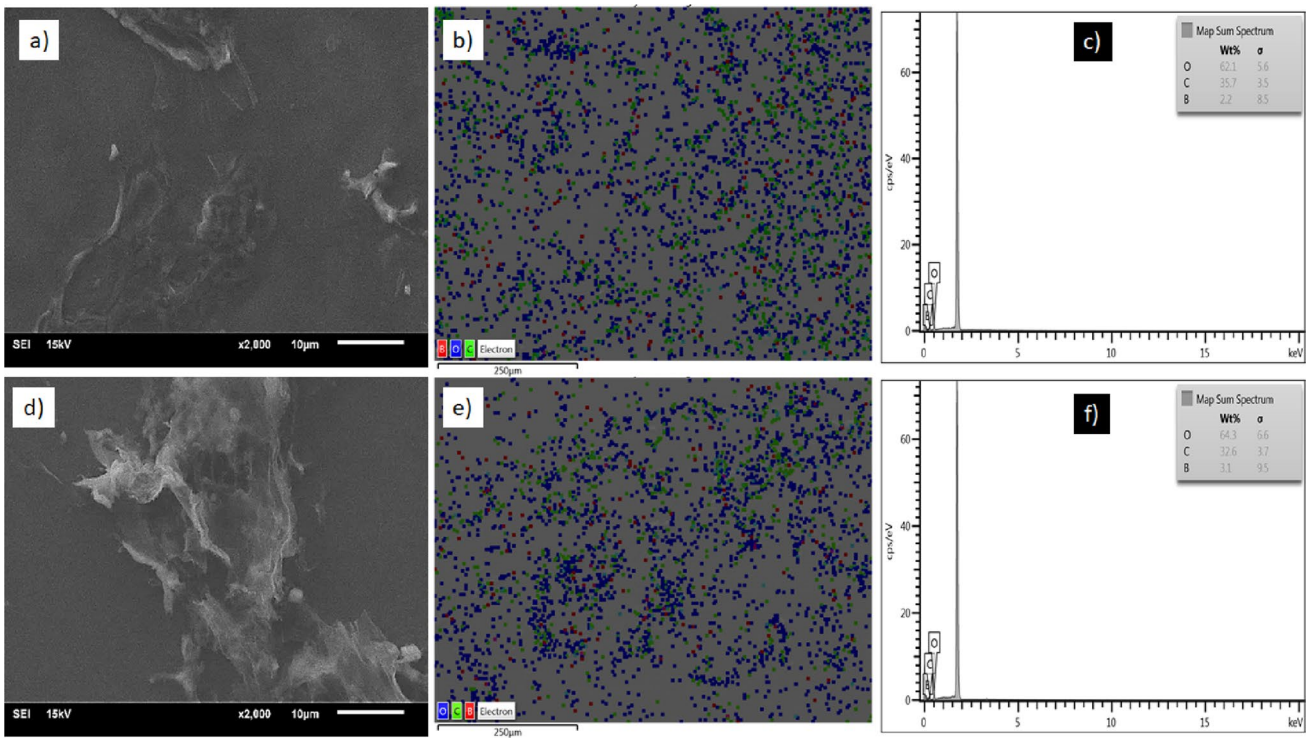

Fig. 6 SEM and EDS analyses of the p-n junction surface. **a** JB1 SEM image, **b** JB1 O, C, B distribution, **c** JB1 map sum spectrum, **d** JB2 SEM image, **e** JB2 O, C, B distribution, **f** JB2 map sum spectrum

the current has to flow laterally to reach the point contact, resulting in a very small cross-sectional area in the current path that is not desirable at all in semiconductor devices.

3.3.2 Capacitance-voltage characteristics of the p-n junctions

The capacitive measurements of the junctions are given in Fig. 8. The capacitance versus the bias voltage measurements were carried out over the range of −3 to 2 V at frequencies from 100 kHz to 10 MHz with one-octave increments.

A small contact (1 mm × 1 mm) on the carbonaceous material and a large contact (5 mm × 5 mm) on silicon substrate suggest that the current flows in a truncated pyramidal volume.

Due to the high resistivity of the carbonaceous material, a significant amount of series resistance may be formed. The resistance R of this volume can be calculated with an integral in Eq. 3

$$R = \int_a^b \frac{\rho}{A(x)} dx \tag{3}$$

where ρ is the resistivity of the carbonaceous material; $A(x)$, the cross-sectional area for the current flow; a, the distance from the small contact plane to the apex of the pyramid; and b, the height of the pyramid. Using the contact dimensions and the thickness of the carbonaceous layer, $A(x)$, a and b can be approximated as follows: $A(x) = 6.25 \times 10^6\, x^2$, $a = 4 \times 10^{-5}$ cm, and $b = 2 \times 10^{-4}$ cm.

$$R = \frac{\rho}{6.25 \times 10^6} \int_a^b \frac{1}{x^2} dx \tag{4}$$

Using the numerical values for resistivity given above and carrying out the integral (Eq. 4), the series resistances are calculated to be $R_{JB1} = 147\ \Omega$ and $R_{JB2} = 166\ \Omega$.

To neglect the effect of the series resistance in the capacitance measurements, the product ωCR must be much smaller than unity ($\ll 1$). From the experiments, the maximum values for the capacitance C (~28 pF can be taken for both JB1 and JB2), the measurement frequency ω (the max frequency of 10 MHz) and the series resistance R (max resistance of 166 Ω) would yield $\omega CR < 2\pi 10 \times 10^6 \times 28 \times 10^{-12} \times 166 = 0.292$ which is not "much smaller" than one. That means, the accuracy of the measurements becomes questionable on the higher side of the frequency range.

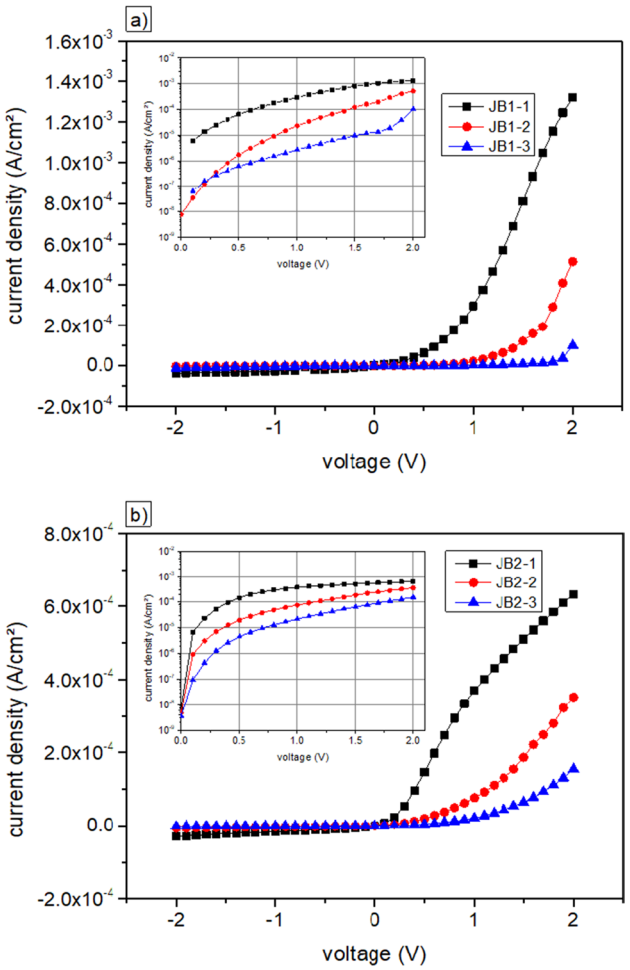

Fig. 7 I-V characteristics of the p-n junctions in linear and semi-logarithmic scales. **a** JB1, **b** JB2

At this stage, the dielectric relaxation time (τ_r), which is calculated as the permittivity (ε) divided by the conductivity (σ) of the material, is of interest $\tau_r = \varepsilon/\sigma = \rho\varepsilon_r\varepsilon_o$, where ε_r is the relative permittivity of the medium, and ε_o is the permittivity of the free space (8.85×10^{-14} Fcm^{-1}). Since the relative dielectric constant for bio-carbon is around 5 [21], the relaxation time for B1 and B2 carbonaceous materials can be estimated to be $\tau_{rB1} = 20.3$ ns and $\tau_{rB2} = 23.0$ ns, respectively. These time scales correspond to 43.5- and 49.2-MHz frequencies, where a maximum capacitance measurement frequency of 10 MHz provides sufficient time for the charges to move to their final destinations.

The capacitance of the structure may be modeled with two parallel-plate capacitors in series—one representing the carbon side while the other representing the silicon side. For a "large" (5 mm × 5 mm) area junction, the measured capacitance is below 28 pF which is rather small. A parallel-plate capacitor of (1 mm × 1 mm) surface area (A_C), which is set by the capacitance meter probe, with the carbonaceous material of 2-µm thickness (d) placed as its dielectric would yield a carbon-side capacitance as given in Eq. 5:

$$C = A_C\frac{\varepsilon_r\varepsilon_o}{d} = 0.01\frac{5\times8.85\times10^{-14}}{2\times10^{-4}} = 22\times10^{-12}F \tag{5}$$

The depletion region width on the silicon side (x_n) may be expressed as in Eq. 6:

$$x_n = \sqrt{\frac{2\varepsilon_r\varepsilon_o}{qN_D}(V_b - V_{an})} \tag{6}$$

where N_D is the doping density; qV_b, the band-bending voltage; and V_{an}, the fraction of the applied voltage occurring on the silicon side. On the silicon side, a band bending around 0.4 V is estimated as being on the n-side of a silicon diode with medium doping. V_{an} has to be less than V_b for consistency. Under zero bias, for $N_D = 2\times10^{14}$ cm^{-3}, $x_n = 2.5\times10^{-4}$ cm; for $N_D = 10^{17}$ cm^{-3}, $x_n = 1.1\times10^{-5}$ cm. The corresponding capacitance values would be 42.4 pF and 963 pF respectively. Placing the silicon side and carbon side capacitances in series, the overall capacitance of the structure under zero bias would be 14.4 pF for the low-doped silicon case, and 21.5 pF for the heavier doped silicon case.

In line with the depletion in silicon, the charge neutrality would require some depletion region in the carbon layer. The "space charge" on the carbon side of the junction per unit area must be equal to the space charge on the silicon side, as shown in Eq. 7:

$$\begin{aligned} |Q^-| &= |Q^+| \\ qx_nN_D &= qx_pN_A \end{aligned} \tag{7}$$

Table 2 Calculated non-linear (1) and piecewise linear model (2) parameters for the samples

Sample	V_1 (V)	V_2 (V)	I_1 (A cm^{-2})	I_2 (A cm^{-2})	n	I_s (A cm^{-2})	V_γ (V)	R_F (Ω)
JB1-1	1.80	0.80	1.16×10^{-3}	1.74×10^{-4}	20.32	3.96×10^{-5}	0.62	1020
JB1-2	2.00	1.30	5.13×10^{-4}	6.52×10^{-5}	13.05	1.42×10^{-6}	1.20	1560
JB1-3	2.00	1.80	1.01×10^{-4}	1.87×10^{-5}	4.56	4.82×10^{-12}	1.75	2430
JB2-1	1.10	0.50	4.01×10^{-4}	1.47×10^{-4}	23.00	7.57×10^{-5}	0.15	2360
JB2-2	2.00	1.00	3.52×10^{-4}	7.65×10^{-5}	25.20	1.75×10^{-5}	0.72	3630
JB2-3	2.00	1.00	1.55×10^{-4}	2.18×10^{-5}	19.60	3.12×10^{-6}	0.84	7510

Table 3 Estimated diode parameters from semilog and linear graphs (Fig. 7a,b)

Sample	I_s (Acm^{-2})	V_γ (V)	R_F (Ω)
JB1-1	8.00×10^{-5}	0.75	911
JB1-2	1.20×10^{-6}	1.50	975
JB1-3	1.60×10^{-7}	1.85	1500
JB2-1	2.40×10^{-4}	0.20	2086
JB2-2	1.80×10^{-5}	0.85	3194
JB2-3	2.50×10^{-6}	1.15	5484

where x_p is the depletion width, and N_A is the effective doping density in the carbonaceous layer. The last equation requires $x_p = x_n N_D/N_A$. Approximating N_A with the hole density (1.1×10^{13} cm^{-3}) in the p-layer, and using the numbers calculated above ($N_D = 2\times10^{14}$ cm^{-3}, $x_n = 2.5\times10^{-4}$ cm), the depletion width in the p-layer is found to be 4.5×10^{-3} cm = 45 μm. The second sample had a hole density of 9.5×10^{12} cm^{-3} yielding a depletion region of 5.26×10^{-4} cm = 5.26 μm. Considering the 2-μm thickness of the p-layer, such a wide depletion region would leave no quasi-neutral region on the p-side of the structure. In other words, the carbonaceous layer is likely to be completely depleted of carriers.

The overall shape of the C-V curves resembles that of a metal-oxide-semiconductor structure (MOS "diode"). For negative voltages, the depletion region is widened in n-type silicon reaching a deep-depletion stage. Negative voltages with a larger absolute value could create an inversion on the silicon surface, thus, increasing the capacitance. The positive bias voltages seem to decrease the

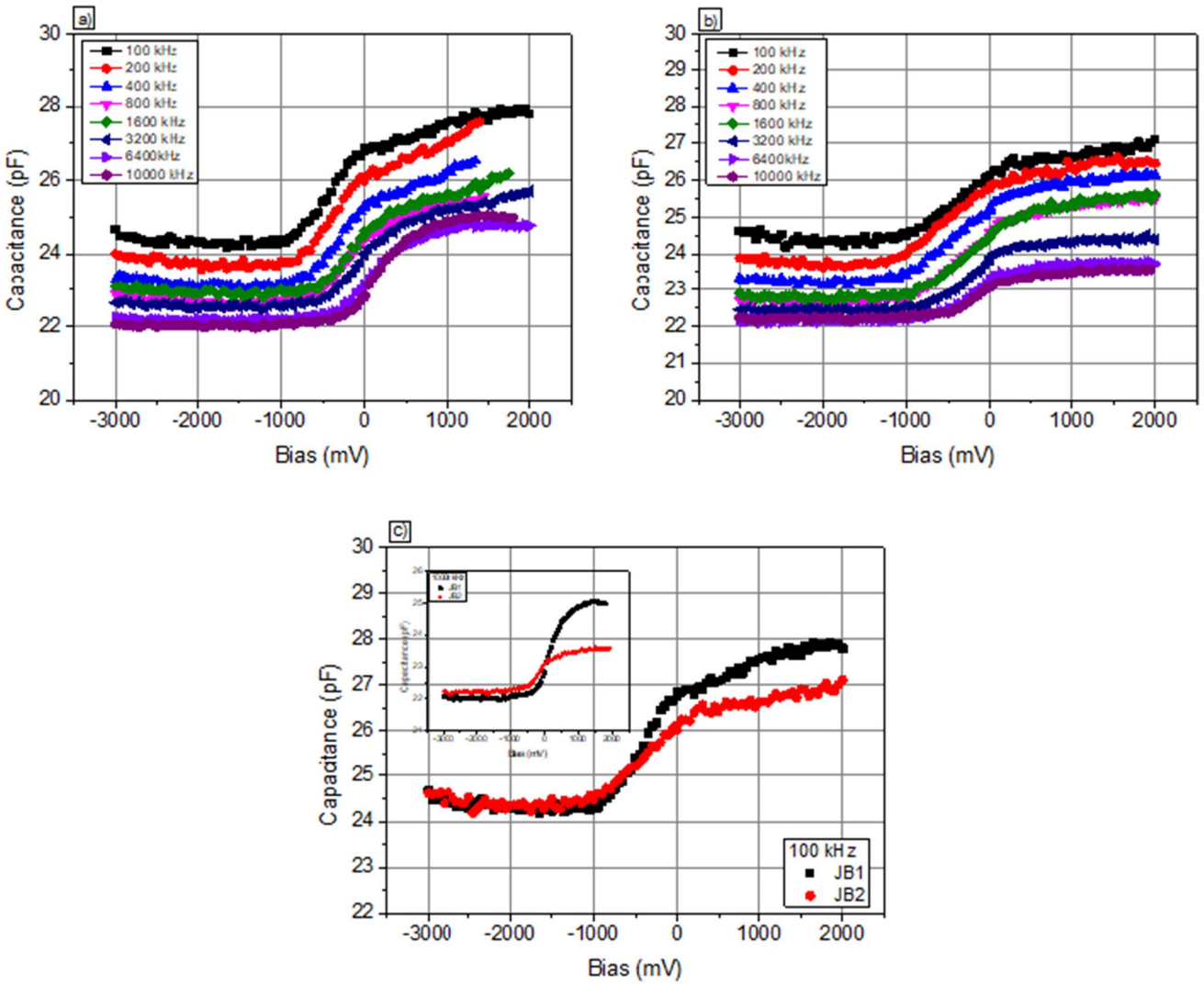

Fig. 8 C-V plots of the junctions at the various frequencies 100 kHz–10 MHz. **a** JB1, **b** JB2, **c** comparing the capacitances at the minimum and maximum frequencies

depletion width on the silicon substrate and further create an accumulation of electrons close to the silicon surface resulting in a higher capacitance value. As the measurement frequency increases, carriers cannot move as fast, resulting in a smaller capacitance.

A forward biased p-n junction would have a significant amount of current, and a diffusion capacitance is associated with the injected excess charge in the quasi-neutral regions. Since the currents are at very low levels, the diffusion capacitance in the samples under study is likely to be insignificant in comparison to the depletion capacitance.

4 Conclusion

The derived carbonaceous materials show semi-conductive properties. Although the structures are not well-crystallized forms of carbon, they could be transformed from non-conductive to semiconductive materials.

The I-V characteristics of the p-type BC on an n-type silicon substrate displayed diode like behavior. Each structure has a different reverse saturation current and cut-in voltage. It could be due to the amorphous and non-uniform nature of the BC layer. Because each sample had a high series resistance, the current levels were low compared to in a traditional silicon p-n junction with a similar junction areas. This would limit the usefulness of these structures as "diodes" that are supposed to act as an open circuit in reverse bias and a short circuit in forward bias with ideally no voltage drop. The C-V characteristics of the structure resemble those of the MOS diode. A much thicker carbonaceous layer may be grown and experimented with for further research.

Studies on the applicability of biomass-derived conductive nanomaterials in electrical/electronic devices (diodes. transistors. electrical circuits, etc.) should be intensified.

Supplementary Information The online version contains supplementary material available at https://doi.org/10.1007/s13399-024-05413-8.

Author contribution G. Akgül planned the study, prepared the bio-carbon material, performed the characterization, formed the device structure and wrote the literature review and the first draft of the manuscript. M. Tomakin performed the material and device characterization and reviewed the manuscript. H. H. Erkaya performed the device analysis and modeling and reviewed the manuscript.

Funding Open access funding provided by the Scientific and Technological Research Council of Türkiye (TÜBİTAK).

Data availability Most of the data is included in the manuscript in graphics form. Details of the data points for the graphics are with the authors in spreadsheet formats.

Declarations

Ethical approval Declaration is not applicable.

Conflict of interest G. Akgül is interested in the growth and usage of the bio-carbon materials. M. Tomakin is interested in the characterization of the device and materials. H. H. Erkaya is interested in the device behavior.

References

1. Vendelin GD, Pavio AM, Rohde UL (2006) Principles of semiconductor devices—book review. IEEE Circuits Devices Mag 22:58–59
2. Kolahdouz M, Xu B, Nasiri AF, Fathollahzadeh M, Manian M, Aghababa H, Wu Y, Radamson HH (2022) Carbon-related materials: graphene and carbon nanotubes in semiconductor applications and design. Micromachines 13:1257
3. Graham AP, Duesberg GS, Hoenlein W, Kreupl F, Liebau M, Martin R, Rajasekharan B, Pamler W, Seidel R, Steinhoegl W, Unger E (2005) How do carbon nanotubes fit into the semiconductor roadmap? Appl Phys A Mater Sci Process 80:1141–1151
4. Zamzami MA, Rabbani G, Ahmad A, Basalah AA, Al-Sabban WH, Ahn SN, Choudhry H (2022) Fabrication and characterization of field effect transistor based on single walled carbon nanotubes. J King Saud Univ-Sci 34
5. Zhang T, Wan X, Huang H, Liu Y, Kang Z (2023) Conventional and inverted light-emitting diodes with 386 nm emission wavelength based on metal-free carbon dots. ACS Appl Mater Interfaces 15(14):18045–18054
6. Huo TT, Zhang DD, Shi XL, Pan Y, Sun LJ, Su YJ (2022) High-performance self-powered photodetectors based on the carbon nanomaterial/GaAs vdW heterojunctions. Chin Opt 15:373–387
7. González D, Montes-Morán MA, Garcia AB (2003) Graphite materials prepared from an anthracite: a structural characterization. Energy Fuels 17:1324–1329
8. Yang L, Chen W, Yu Q, Liu B (2021) Mass production of two-dimensional materials beyond graphene and their applications. Nano Res 14:1583–1597
9. Xu C, Nasrollahzadeh M, Selva M, Issaabadi Z, Luque R (2019) Waste-to-wealth: biowaste valorization into valuable bio(nano) materials. Chem Soc Rev 48:4791–4822
10. Tiwari SK, Bystrzejewski M, De Adhikari A, Huczko A, Wang N (2022) Methods for the conversion of biomass waste into value-added carbon nanomaterials: recent progress and applications. Prog Energy Combust Sci 92:101023
11. Tamuly J, Bhattacharjya D, Saikia BK (2022) Graphene/graphene derivatives from coal, biomass, and wastes: synthesis, energy applications, and perspectives. Energy Fuels 36(21):12847–12874

12. Pang YL, Lim CW, Pui K, Shak Y, Lim S, Cheam WC, Koo CH, Abdullah AZ (2020) Biomass-based photocatalysts for environmental applications, nanophotocatalysis and environmental applications-environmental chemistry for a sustainable world, vol 30. Springer, Cham, pp 55–86
13. Serafin J, Ouzzine M, Xing C, El Ouahabi H, Kaminska A, Srenscek-Nazzal J (2022) Activated carbons from the Amazonian biomass andiroba shells applied as a CO2 adsorbent and a cheap semiconductor material. J CO2 Util 62:102072
14. Villarreal CC, Monge S, Aguilar D et al (2022) Bio-sensitized solar cells built from renewable carbon sources. Mater Today Energy 23:100910
15. Meng W, Wang B, Ai L, Song H, Lu S (2021) Engineering white light-emitting diodes with high color rendering index from biomass carbonized polymer dots. J Colloid Interface Sci 598:274–282
16. Gong Y, Han Y, Zhang F, Zhai M, Chen X, Long Q, Wang Z, Chen F, Yang J (2020) Color tuning of biomass-derived carbon nanodots by reaction temperature toward white light-emitting diodes. NANO 15(12):2050159
17. Akgül G, Sözer S (2023) A PN junction application of renewable carbon derived from tea waste biomass on a silicon substrate. Pamukkale Univ J Eng Sci 29:146–150
18. Karamustafa A, Sözer S, Oskay KO, Buldu-Akturk M, Erdem E, Akgül G (2022) Improving the electrochemical energy storage capacity of the renewable carbon derived from industrial tea waste. Russ J Electrochem 58:844–854
19. Akgül G, Bıçakçı SN (2020) Optical and electrical properties of refined carbon derived from industrial tea waste. Mater Res Express 7:3–12
20. Akgül G, Iglesias D, Ocon P, Moreno Jiménez E (2019) Valorization of tea-waste biochar for energy storage. Bioenergy Res 12:1012–1020
21. Paredes JI, Villar-Rodil S, Martínez-Alonso A, Tascón JMD (2008) Graphene oxide dispersions in organic solvents. Langmuir 24:10560–10564
22. Konios D, Stylianakis MM, Stratakis E, Kymakis E (2014) Dispersion behaviour of graphene oxide and reduced graphene oxide. J Colloid Interface Sci 430:108–112
23. Mohandoss M, Nelleri A (2018) Optical properties of sunlight reduced graphene oxide using spectroscopic ellipsometry. Opt. Mater. (Amst). 86:126–132. https://doi.org/10.1016/j.optmat.2018.09.035.
24. Klein CA, Straub WD (1961) Carrier densities and mobilities in pyrolytic graphite. Phys Rev 123(5):1581–1583